Nighttime Multilayered Cloud Detection Using MODIS and ARM Data

BRYAN A. BAUM

NASA Langley Research Center, Hampton, Virginia

RICHARD A. FREY

Cooperative Institute for Meteorological Satellite Studies, University of Wisconsin—Madison, Madison, Wisconsin

GERALD G. MACE

University of Utah, Salt Lake City, Utah

MONICA K. HARKEY

University of Wisconsin—Madison, Madison, Wisconsin

PING YANG

Texas A&M University, College Station, Texas

(Manuscript received 3 June 2002, in final form 10 January 2003)

ABSTRACT

This study reports on recent progress toward the discrimination between pixels containing multilayered clouds, specifically optically thin cirrus overlying lower-level water clouds, and those containing single-layered clouds in nighttime Moderate Resolution Imaging Spectroradiometer (MODIS) data. Cloud heights are determined from analysis of the 15-μm CO_2 band data (i.e., the CO_2-slicing method). Cloud phase is inferred from the MODIS operational bispectral technique using the 8.5- and 11-μm IR bands. Clear-sky pixels are identified from application of the MODIS operational cloud-clearing algorithm. The primary assumption invoked is that over a relatively small spatial area, it is likely that two cloud layers exist with some areas that overlap in height. The multilayered cloud pixels are identified through a process of elimination, where pixels from single-layered upper and lower cloud layers are eliminated from the data samples. For two case studies (22 April 2001 and 28 March 2001), ground-based lidar and radar observations are provided by the Atmospheric Radiation Measurement (ARM) Program's Southern Great Plains (SGP) Clouds and Radiation Test Bed (CART) site in Oklahoma. The surface-based cloud observations provide independent information regarding the cloud layering and cloud height statistics in the time period surrounding the MODIS overpass.

1. Introduction

Cloud layering poses a challenge to the proper retrieval of cloud microphysical and macrophysical properties in satellite imagery, especially at night. This study builds upon previous research (Baum et al. 1994) on the nighttime analysis of satellite imagery containing cirrus over boundary layer water clouds. The previous effort was based on data merged from two instruments on the National Oceanic and Atmospheric Administration (NOAA) operational polar-orbiting platforms, namely the Advanced Very High Resolution Radiometer (AVHRR) and the High Resolution Infrared Radiometer Sounder (HIRS/2). The upper-cloud properties were derived from the HIRS sounder data, while the low-level water cloud properties were determined primarily from the AVHRR data. Besides the complexities inherent in merging data from two instruments, the ability to infer the phase of each cloud layer was problematic, and the cirrus-scattering models were simplistic in comparison with what is currently available. In this study, we describe a more effective and straightforward approach for the detection of cirrus overlying lower-level water clouds in nighttime imagery using multispectral data from the Moderate Resolution Imaging Spectrometer (MODIS). Our eventual goal is to facilitate the development of operational methods to discern where multilayered clouds exist in nighttime MODIS imagery.

The methodology improvements we report here stem

Corresponding author address: Dr. Bryan A. Baum, NASA/CIMSS, 1225 W. Dayton St., Madison, WI 53706.
E-mail: bryan.baum@ssec.wisc.edu

primarily from the availability of more realistic cirrus-scattering models and the use of operational MODIS products that provide information on whether each pixel contains clouds (i.e., a cloud mask), cloud thermodynamic phase, and cloud height. Cloud phase is inferred from analysis of the 8.5- and 11-μm data (Strabala et al. 1994; Baum et al. 2000b). The cirrus-scattering models have also advanced since the earlier study by Baum et al. (1994) and are now based on mixtures of randomly oriented hexagonal plates and columns, two-dimensional bullet rosettes, and aggregates.

Multilayered, overlapping clouds are often found in the storm tracks of the North Atlantic and Pacific Oceans as well as in the vicinity of the intertropical convergence zone (ITCZ; Hahn et al. 1982, 1984). Tian and Curry (1989) combined satellite, aircraft, and surface observations in the North Atlantic Ocean to infer cloud overlap statistics, although their data was limited in vertical resolution. Their study found that cloud-layer overlap in adjacent grid levels in a column can be considered as having maximum overlap, while cloud layers separated by clear (noncloudy) levels should assume random overlap.

The most common cloud-layering schemes (e.g., Chou et al. 1998; Hogan and Illingworth 2000) include (a) random overlap, in which clouds are assumed to be randomly distributed horizontally at each level; (b) mixed overlap, in which all clouds are randomly overlapped except for convective clouds, which are maximally overlapped; (c) maximum overlap, in which all clouds are overlapping as much as possible; and (d) combinations of these overlap assumptions. In the maximum–random assumption, vertically continuous clouds are assumed to be maximally overlapped, while clouds separated by levels without clouds are assumed to have random overlap.

Ground-based measurements by active sensors of vertical cloud layering have been analyzed in the midlatitudes (Uttal et al. 1995) as well as in the Arctic (Intrieri et al. 2002). In the United Kingdom, Hogan and Illingworth (2000) used 71 days of cloud data from a 94-GHz high-vertical-resolution radar to investigate the various cloud overlap assumptions employed in global climate models (GCMs). They found that the overlap between cloud layers tends to fall rapidly as their vertical separation increases. This approach was explored further by Mace and Benson-Troth (2002) using 103 months of continuous millimeter cloud radar measurements obtained from the Atmospheric Radiation Measurement (ARM) sites in the Tropics, the North Slope of Alaska, and the southern Great Plains (SGP). While this study supported the assumption of random overlap for layers separated by clear (noncloudy) layers, they found that the overlap characteristics of vertically continuous layers cannot always be considered as maximal, and further found that the overlap characteristics seem to be seasonally dependent.

The cloud overlap assumption used in a GCM affects the results of the model (Liang and Wang 1997; Stubenrauch et al. 1997; Weare 2001; Chen et al. 2000; Morcrette and Jakob 2000), making the basis of the assumption critical for radiative feedback and heating calculations. Cloud overlap assumptions have also been shown to affect the modeled precipitation rates (Jakob and Klein 1999). Weare (2001) explored the effects of two different overlap treatments in the column radiative model (CRM) of the National Center for Atmospheric Research (NCAR) Community Climate Model (CCM). The two cloud overlap models that were used involved 1) the random cloud overlap assumption and 2) a ''nonrandom'' model that specifies cloud overlap from satellite and surface observations inferred from monthly, not daily or instantaneous, cloud observations (Weare 1999). Weare presents his results in terms of the changes in net cloud radiative forcing (netCRF) resulting from changes in total cloud water or increases in low, middle, and high cloud-layer fraction amounts. The random model results indicate that netCRF is more sensitive to increases in low clouds than the nonrandom model. However, the nonrandom model results show netCRF to be more sensitive to increases in the middle cloud-layer fractional amount.

With such far-ranging effects, improvements in the remote sensing of multilayered clouds are crucial so that GCMs may have a basis for testing their treatment of multiple cloud layers. It would be especially useful, at some point in the future, to have a global satellite-based dataset of overlapping cloud occurrences to compare with GCM model results.

The primary goal of this study is to suggest an approach to discriminate between pixels that contain a single cloud layer from those that potentially contain overlapping cloud layers in nighttime MODIS data. First, theoretical calculations are presented to provide a framework for the interpretation of the MODIS data. Subsequently, two case studies are presented in detail. For the first case study, 22 April 2001, data are analyzed from single-layered cirrus and single-layered water clouds, as well as from a more complex multilayered cloud region. The second case study, 28 March 2001, provides another example of our methodology. To support the interpretation of complex MODIS imagery, supplemental data are provided from ground-based radar and lidar instruments located at the Department of Energy (DOE) ARM Clouds and Radiation Test Bed (CART) SGP site. The ground-based instrumentation provides insight as to the time history of the cloud layers for the temporal period encompassing the MODIS overpass. Section 2 discusses the various datasets and radiative transfer models used in this study. Section 3 provides an outline of the theoretical models that provide the basis for the interpretation of the data. In Section 4, the method of cloud overlap detection is applied to the MODIS nighttime scenes recorded on 22 April 2001, and 28 March 2001. Section 5 concludes.

TABLE 1. MODIS *Terra* spectral bands used in this study, including bandwidths, principal absorbing components, and approximate pressure level corresponding to the peak in the individual band-weighting functions.

MODIS bandnumber	MODIS bandwidth (μm)	Principal absorbing components	Approximate peak in weighting function (hPa)
20	3.66–3.84	H_2O, CO_2, CH_4	Surface
29	8.40–8.70	H_2O, O_3, CH_4, N_2O	Surface
31	10.78–11.28	H_2O, CO_2	Surface
33	13.19–13.49	H_2O, CO_2	900
34	13.49–13.79	H_2O, CO_2	700
35	13.79–14.09	CO_2	500
36	14.09–14.39	CO_2	300

2. Data and models

a. MODIS data products

MODIS is the primary imager on the Earth Observing System's *Terra* platform. The *Terra* satellite is in a sun-synchronous, near-polar orbit of 705 km and views the entire surface of the earth every 1–2 days (Salomonson et al. 1989). MODIS obtains radiometric measurements in 36 spectral bands ranging from 0.4 to 14.4 μm. The bands used in this study and their characteristics are shown in Table 1. Pixels unobstructed between the surface and the satellite are determined using the operational procedures discussed in Ackerman et al. (1998).

1) CLOUD HEIGHT AND TEMPERATURE (CO_2 SLICING)

The technique to infer cloud-top pressure and effective cloud amount (the cloud fraction multiplied by the emittance at 11 μm) has been discussed in detail by Menzel et al. (1983) and Wylie and Menzel (1999). Error analyses for the method are provided in Wielicki and Coakley (1981), Menzel et al. (1992), and Baum and Wielicki (1994). The method takes advantage of differing partial CO_2 absorption in several of the MODIS infrared bands located within the 15-μm CO_2 band, with each band being sensitive to a different level in the atmosphere. The bands located closer to the center of the CO_2 band at 15 μm are sensitive to high clouds only, while the bands away from the CO_2-band center are sensitive also to the presence of midlevel clouds.

Retrievals are derived from ratios of radiance differences between cloudy and clear-sky regions at two nearby wavelengths. The CO_2-slicing method has been used in operational processing of the Geostationary Operational Environmental Satellite (GOES) and HIRS data, and has been found to have accuracies of approximately 50 hPa for clouds at heights above 3 km (approximately 700 hPa). The MODIS operational method was tested using MODIS Airborne Simulator data and was compared with airborne lidar measurements (Frey et al. 1999), with similar accuracies as stated above. The cloud height accuracy increases as the cloud optical thickness increases and is most problematic for optically thin cirrus. Because of signal-to-noise issues, cloud heights inferred from the method must be in the range from approximately 700 hPa to the tropopause. If no valid retrieval is found in this pressure range, the 11-μm band is used to infer cloud pressure, assuming the cloud is opaque.

In MODIS operational processing, cloud-top pressures are calculated for the following ratio pairs: 14.2/13.9, 13.9/13.6, 13.6/13.3, 13.9/13.3, and 13.3 μm/11 μm. Previous studies have not included the 13.3-μm/11-μm band pair, but its use is restricted to ice clouds only. Given the fact that each band pair may return a different cloud pressure and effective cloud amount, a choice must be made as to the most representative cloud pressure. The final cloud pressure is chosen by minimizing the difference between the observed cloud signal (i.e., the difference between the clear-sky and measured radiance) and the simulated cloud signal calculated from a forward radiative transfer model (Menzel et al. 1983).

2) CLOUD PHASE

Cloud phase is inferred from measurements at 8.5- and 11-μm (Strabala et al. 1994; Baum et al. 2000b). Radiative transfer (RT) simulations (following Baum et al. 2000a,b) indicate that the brightness temperature difference (BTD) between the 8.5- and 11-μm bands [hereinafter denoted as BTD(8.5–11)] tends to be positive in sign for ice clouds that have an infrared optical thickness greater than approximately 0.5. Water clouds of relatively high optical thickness tend to exhibit highly negative BTD(8.5–11) values of less than -2 K. The BTD(8.5–11) values are quite sensitive to atmospheric absorption, especially by water vapor, and also to the surface emittance properties. Clear-sky BTD(8.5–11) values tend to be negative because the surface emittance at 8.5 μm tends to be much lower than at 11 μm, especially over nonvegetated surfaces. The BTD value for low-level water clouds tends to become more negative as the water vapor loading increases. While a relatively small effect, multiple scattering is included in radiative transfer simulations of the BTD(8.5–11). Small particles tend to increase the BTD(8.5–11) values relative to large particles because of increased scattering. These effects are discussed in more detail in section 3c.

There are two primary issues that cause difficulties

for the IR phase method. First, optically thin cirrus are very difficult to detect, much less to discern the phase unambiguously. Second, the ability to discriminate between ice and water particles at cloud top is much reduced when clouds may contain primarily supercooled water droplets or perhaps a mixture of both ice and water (i.e., mixed phase). Single-layered clouds of wide spatial extent having cloud-top temperatures in the range between 233 and 273 K are prevalent in the storm tracks in both the Northern and Southern Hemispheres. Efforts are ongoing to ameliorate these known problems.

b. ARM CART site cloud products

The 35-GHz millimeter cloud radars (MMCR; Moran et al. 1998) at the ARM central facility are a vertically pointing system designed to map the distribution of clouds and precipitation in the vertical column above the instruments. The MMCR uses relatively low peak-power transmitters (100 W), a high duty cycle (25%), and large antennas (57.2 dB gain at SGP) that allow for high sensitivity (approximately -50 dBZ_e at 5 km). The sensitivity of the MMCR over a wide range of cloud types is attributable to the design of the signal-processing system. The radar is cycled through four distinct modes, each targeted to sense optimally a different class of hydrometeor in a procedure described by Clothiaux et al. (1999).

The standard operational modes of the MMCR are combined into a single dataset with 90-m vertical resolution and ~35-s temporal resolution. Cloud boundaries are generated from a binary description of significant echo return in the time–range domain of the data using a cloud-masking algorithm similar to that described by Clothiaux et al. (1995). The masking algorithm is applied to each mode sequentially and the masks are then combined following Clothiaux et al. (2000). Additionally, at the SGP site the sensitivity of the radar in the lower range gates often leads to significant return due to nonhydrometeor targets, such as insects. To discriminate between cloud and other scatterers, the radar mask is combined with observations from collocated laser ceilometers and lidars. This aids in discriminating between cloud and precipitation in the lowest hydrometeor layer because the laser instruments do not typically identify precipitation because of the generally low optical path associated with precipitation and the tuning of the ceilometer algorithm thresholds.

3. Models

a. Cloud microphysical models

Because these models have been discussed previously (Baum et al. 2000a), only a brief discussion is provided herein. Water phase clouds are treated as being composed of a modified gamma distribution of droplets having effective radii (r_{eff}) ranging from 4 to 12 μm with an effective variance of 0.1. Mie theory is used to provide the optical properties for each distribution, including the scattering phase function, single scatter albedo (ω), and extinction cross section.

Cirrus microphysical and optical properties are used from four separate models based on in situ cirrus measurements. The four models follow the cold cirrus, cirrostratus, cirrus at $T = -40$°C, and cirrus uncinus distributions (Baum et al. 2000a). The optical properties for these four cirrus microphysical models are computed for a mixture of habits including hexagonal plates, hollow columns, two-dimensional bullet rosettes, and aggregates.

b. Treatment of atmospheric absorption

MODIS radiances are influenced by atmospheric (molecular) absorption, the presence of clouds and/or aerosols and their type(s), and surface properties. In this study, the effects of aerosols are not included. A set of correlated-*k* routines developed specifically for the MODIS channels are used to account for molecular absorption. These routines employ an exponential-sum fitting of transmissions (ESFT) technique (Kratz 1995; Kratz and Rose 1999) and are accurate to within 1% for clear-sky conditions when compared with line-by-line calculations. The temperature, relative humidity, dry-bulb temperature, pressure, and altitude data used for calculating atmospheric absorption are provided by rawinsonde data from the SGP site.

c. Radiative transfer simulations

Radiative transfer calculations for both single-layered and multilayered clouds are based on the discrete ordinates model (DISORT; Stamnes et al. 1988). Details on the implementation of the DISORT model may be found in Baum et al. (1994, 2000a). In our implementation, the atmosphere is composed of 34 discrete homogeneous layers. An optical thickness and single scattering albedo are provided for each layer. The clear-sky optical thickness profile is generated using the method in section 3b. Cloud layer optical thicknesses are defined at 11 μm, given by τ_{IR}.

1) WATER-PHASE CLOUD SIMULATIONS

Simulations of water clouds are provided to gain some insight into the behavior of the BTD(3.78–11) and BTD(8.5–11) values as a function of 11-μm brightness temperature (BT). Figure 1 shows such simulations for the case of a cloud at a constant temperature of 273 K but where the effective radius varies from 4 to 12 μm. The effect of changing effective radius is more pronounced for the BTD(3.78–11) values (Fig. 1a) than for the BTD(8.5–11) values (Fig. 1b). The BTD(3.78–11) values increase with increasing r_{eff}. The BTD(3.78–11) values are positive over much of the optical thickness

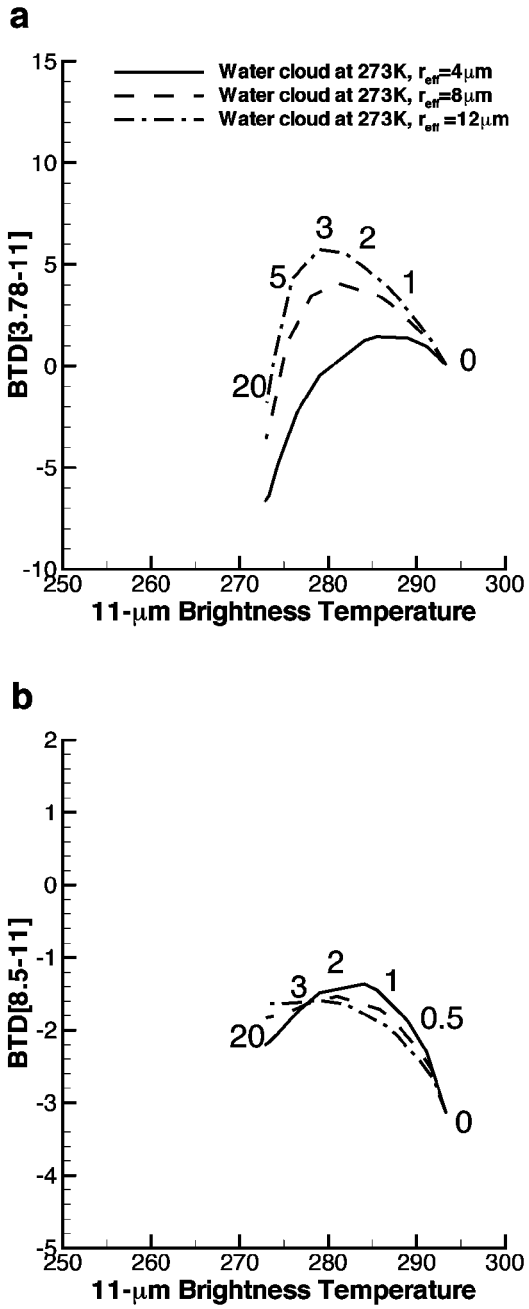

FIG. 1. Dependence of r_{eff} on brightness temperature differences as a function of 11-μm brightness temperature for water-phase cloud at a temperature of 273 K. Calculations are performed for (a) BTD(3.78–11) vs 11-μm brightness temperature and (b) BTD(8.5–11) vs 11-μm brightness temperature. The simulations were performed using a midlatitude summer atmosphere. Infrared cloud-layer optical thickness values (τ_{IR}) are provided on the uppermost curve for reference.

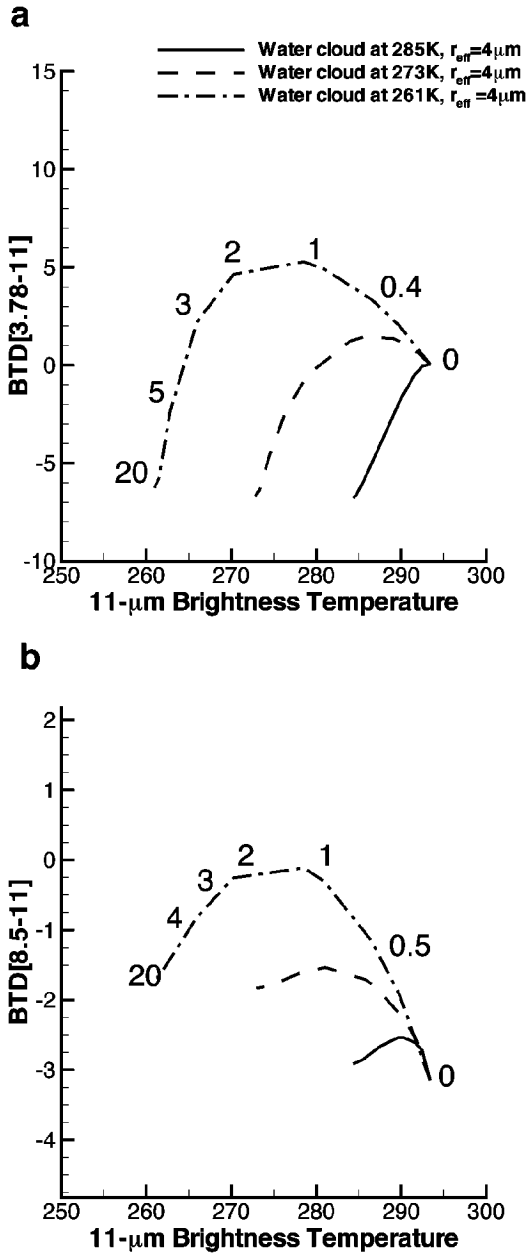

FIG. 2. Dependence of cloud temperature on brightness temperature differences as a function of 11-μm brightness temperature for water-phase clouds at temperatures of 285, 273, and 261 K. Calculations are performed for (a) BTD(3.78–11) vs 11-μm brightness temperature and (b) BTD(8.5–11) vs 11-μm brightness temperature. The simulations were performed using a midlatitude summer atmosphere. Infrared cloud-layer optical thickness values (τ_{IR}) are provided on the uppermost curve for reference.

range, but become negative at high optical thicknesses. The BTD(8.5–11) values remain negative in sign over the entire optical thickness range. Note that the BTD(8.5–11) values display a slight dependence on r_{eff}, but the curves cross between optical thicknesses of 2 and 3. Thus, the BTD(8.5–11) combination is not useful for inference of particle size for water clouds.

The behavior of the BTD values at three cloud temperatures (261, 273, and 285 K) is shown in Fig. 2. In these simulations the effective radius is held constant at 4 μm. Optically thin clouds tend to have the most positive BTD(3.78–11) values, whereas at high optical

thicknesses, the BTD(3.78–11) tends toward negative values. The BTD(8.5–11) values show a marked dependence on cloud temperature. For a midlevel water cloud at 261 K, the BTD(8.5–11) values are negative in sign.

2) ICE-PHASE CLOUD SIMULATIONS

Cirrus cloud simulations are shown in Figs. 3 and 4. Figure 3 shows BTD(3.78–11) and BTD(8.5–11) values as a function of the 11-μm brightness temperature for a fixed cloud temperature of 235 K. Results are shown for four cirrus models. The BTD(3.78–11) values show some dependence on the effective diameter of the cirrus model. The BTD(3.78–11) values tend to decrease as the effective diameter increases for these cirrus models, in contrast to the water cloud results in which the BTD(3.78–11) values increase as r_{eff} decreases. Only at very high optical thicknesses do the BTD(3.78–11) values tend toward zero, and a maximum value occurs at an optical thickness of approximately 3. The BTD(8.5–11) values (Fig. 3b) are negative for both the optically thin cloud and optically thick cloud but are positive over some range of optical thicknesses. In contrast to the water-cloud results of the previous section, optically thin cirrus tend to have positive BTD(8.5–11) values. This feature is what provides the basis for making the inference of cloud phase feasible with the 8.5- and 11-μm bands. Similar to the water-cloud results, the BTD(8.5–11) cirrus simulations show that this band combination is not useful for inferring particle diameter at optical thicknesses larger than approximately 3.

The dependence of the BTD(3.78–11) and BTD(8.5–11) values on cloud temperature is shown in Fig. 4. Both BTD(3.78–11) and BTD(8.5–11) show a marked dependence on the cloud temperature. The dynamic ranges of both the BTD(3.78–11) and BTD(8.5–11) values increase as the cloud temperature decreases. The discrimination between ice- and water-phase clouds becomes less discernable as the cloud temperature approaches that of a midlevel cloud (i.e., 261 K). In practice, determination of cloud phase is problematic for clouds with temperatures between approximately 233 and 273 K.

3) OVERLAPPING CLOUD SIMULATIONS

The intent of this section is to gain some insight as to the relationship between the BTD(3.78–11) and 11-μm brightness temperatures when cirrus overlies a low-level water cloud. Results of one set of simulations are shown in Fig. 5 for the case when a cirrus cloud (using the cold cirrus model) at 235 K overlies a water cloud at 285 K with optical properties based on an effective radius of 4 μm. Infrared optical thicknesses are provided for reference. The water-cloud calculations assume a single-layered cloud, with no overlying cirrus. For reference, the uppermost cirrus curve represents simulated BTD(3.78–11) and 11-μm brightness temperatures for a single-layered cold cirrus cloud with no underlying water cloud. The point where the two curves intersect

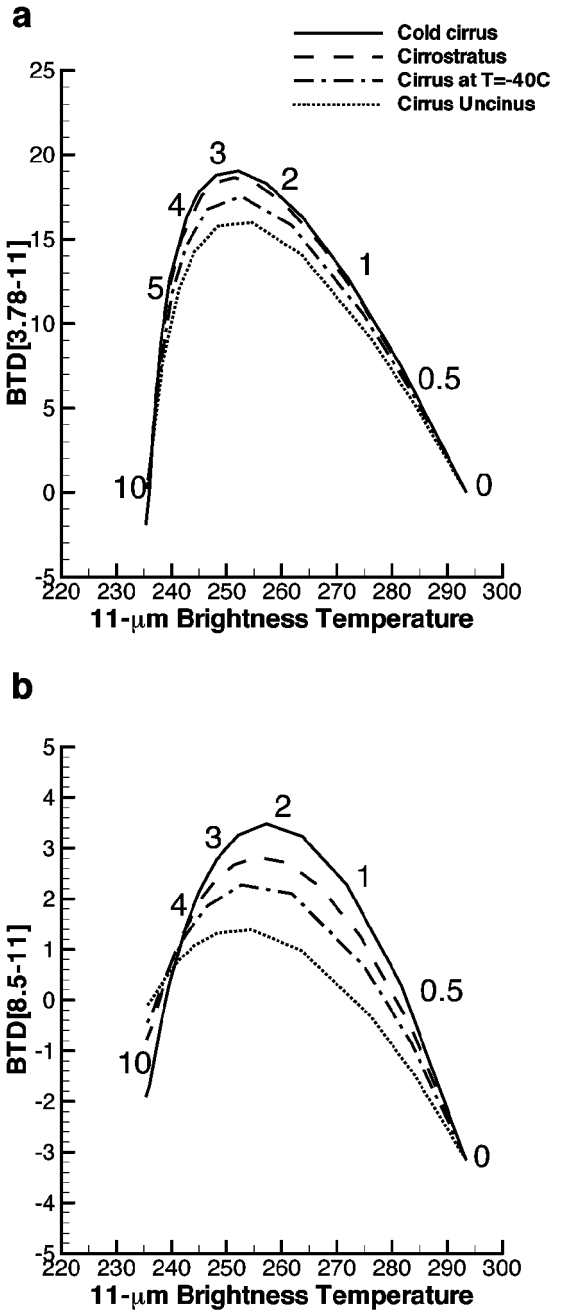

FIG. 3. Dependence of brightness temperature differences as a function of 11-μm brightness temperature for various cirrus models for a cloud at a temperature of 235 K. Calculations are performed for (a) BTD(3.78–11) vs 11-μm brightness temperature and (b) BTD(8.5–11) vs 11-μm brightness temperature. The simulations were performed using a midlatitude summer atmosphere. Four cirrus-scattering models are employed: cold cirrus, cirrostratus, cirrus at T = 40°C, and cirrus uncinus. Infrared cloud-layer optical thickness values (τ_{IR}) are provided on the uppermost curve for reference.

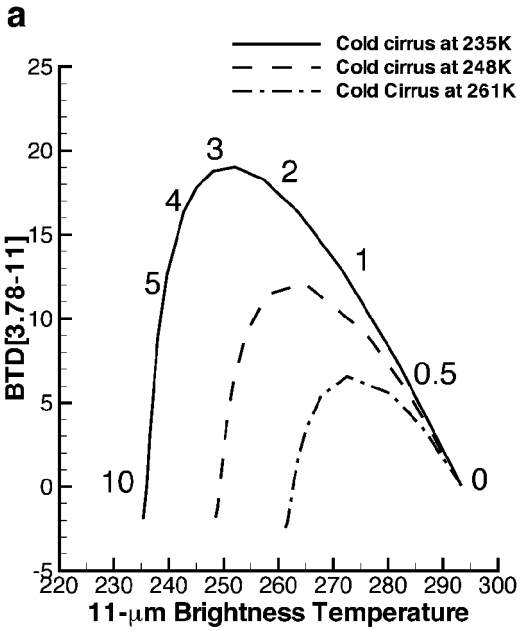

FIG. 4. Dependence of cloud temperature on brightness temperature differences as a function of 11-μm brightness temperature for ice-phase clouds at temperatures of 235, 248, and 261 K. Calculations are performed for (a) BTD(3.78–11) vs 11-μm brightness temperature and (b) BTD(8.5–11) vs 11-μm brightness temperature. The simulations were performed using the cold cirrus-scattering model and a midlatitude summer atmosphere. Infrared cloud layer optical thickness values (τ_{IR}) are provided on the uppermost curve for reference.

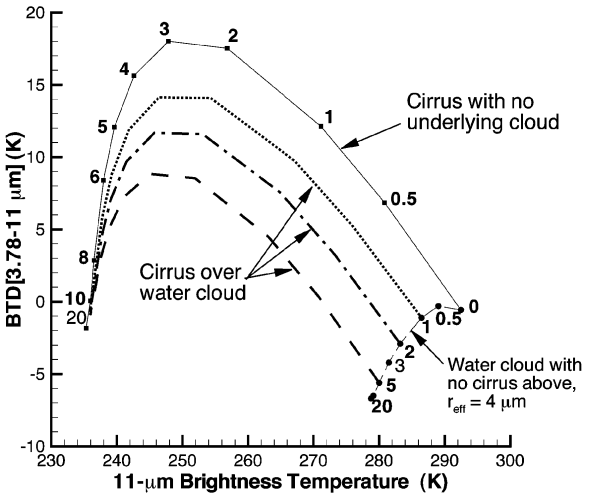

FIG. 5. Simulation of overlapping clouds (cirrus uncinus overlying a low-level water cloud) on brightness temperature differences as a function of 11-μm brightness temperature. The cirrus uncinus and water cloud temperatures are 235 and 285 K, respectively. Infrared cloud-layer optical thickness values (τ_{IR}) are provided on the uppermost cirrus curve and the water-cloud curve for reference.

denotes the region corresponding to clear-sky conditions.

Superimposed on this figure are three additional curves, all based on the cold cirrus model, overlying the lower-level water cloud. The three curves are based on various water-cloud optical thicknesses held constant at values of 1, 2, and 5. As the optical thickness of the water cloud increases, the BTD(3.78–11) values for a range of cirrus optical thicknesses decrease from their single-layered cirrus values when the cirrus cloud is nonopaque. As an example, for a cirrus cloud having an optical thickness of 2 and overlying a water cloud having an optical thickness of 5, the BTD(3.78–11) value decreases from 17 to 7 K.

Should a data point fall within these curves shown for both single- and multilayered clouds, it will be problematic to ascribe the properties of both cloud layers given the limited multispectral data available. Without an active sensor, there is little chance of deciphering the contribution of the upper cloud from the lower cloud, or even of determining whether other cloud layers are present between the uppermost and lowermost layers. What one can assess, however, is that the data may be from an area of potentially overlapping cloud layers, and that the retrievals of cloud height and other properties will have inherently larger errors than those from single-layered cloud systems.

We now extend the analyses reviewed in this section relating the dependencies of the BTD(3.78–11) values to two case studies: 22 April 2001 and 28 March 2001.

4. Methodology and case study results

a. Case study: 22 April 2001

On 22 April 2001 MODIS recorded data over the ARM SGP site at 0450 UTC, and a 3.78-μm image of the scene is provided in Fig. 6. The cloud system observed by MODIS and the ARM SGP instrumentation

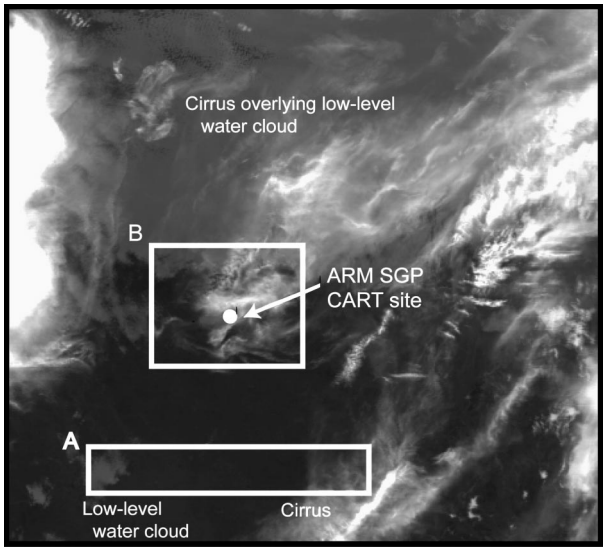

FIG. 6. MODIS 3.78-μm image of a complex nighttime scene recorded at 0450 UTC 22 Apr 2001. Two regions are outlined in the figure. Region A includes data from two cloud layers (low-level water cloud and cirrus) that do not overlap. The size of region A is 0.35° in latitude by 2.2° in longitude. Region B encompasses the ARM CART site and contains both single-layered and multilayered clouds. The size of region B is 0.9° in latitude by 1.3° in longitude.

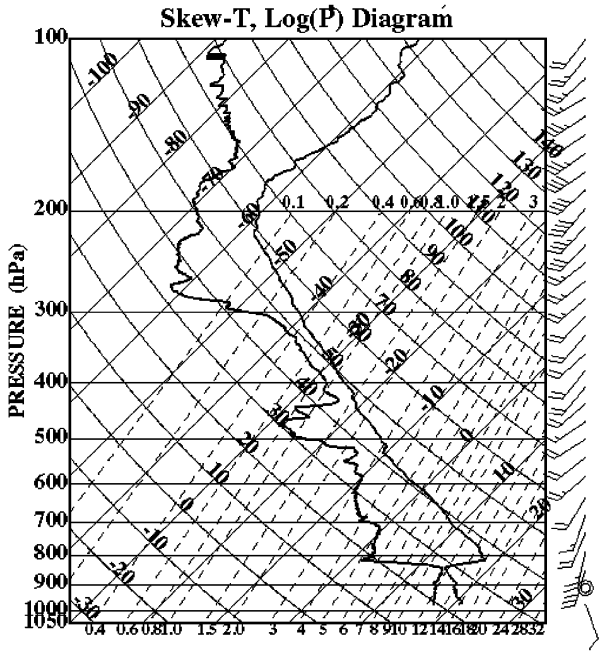

FIG. 7. Skew T–log$p$ diagram from the sounding launched at 0535 UTC 22 Apr 2001. Pressure is denoted along the ordinate (hPa) while temperature (°C) extends diagonally from the lower left-hand to the upper right-hand side. The curved solid lines that run from the upper right-hand to lower left-hand side are the water saturation mixing ratio (g kg^{-1}), while mixing ratio lines (g kg^{-1}) are dashed. Wind barbs are shown with short tick marks denoting 5 m s^{-1} and long ticks denoting 10 m s^{-1}.

formed in association with a vigorous and rapidly propagating low pressure system that moved from southwest to northeast across the Great Plains states on the night of 22 April 2001. By the time of the MODIS overpass, the center of low pressure was already well to the northeast of the SGP central facility near Lamont, Oklahoma, and a slot of dry air was beginning to invade the region behind a frontal system that ran through eastern Oklahoma. The sounding (Fig. 7) launched at 0535 UTC shows that a deep southwesterly flow would have moved clouds at all levels toward the northeast. The sounding also shows a thin, nearly saturated layer near 850 hPa below a strong temperature inversion. The low-level moist layer has a temperature of approximately 288 K. Also evident is a upper-level moist layer based near 430 hPa (approximately 6 km) and having a temperature of 255 K. This higher moist layer appears to have been fairly deep, judging by the sounding data.

In Fig. 6, two regions have been chosen to illustrate our methodology for the detection of multilayered cloud pixels. Region A encompasses an area south of the ARM SGP CART site. These data were selected because the area contains two cloud layers that do not overlap. A scatterplot of the BTD(3.78–11) versus 11-μm BT data are shown in Fig. 8a. The pixels associated with clear-sky (red), ice cloud (blue), and water cloud (green) are identified in Fig. 8b. Clear-sky pixels, defined as the pixels that are unobstructed between the surface and the satellite, are determined from application of the MODIS operational cloud-clearing algorithm (Ackerman et al. 1998). We note that some of the pixels classified as being water phase are located along the pixel distribution associated with the cirrus, and are likely misclassified. Further analysis indicates that most of these pixels tend to be located at the boundaries of the cirrus clouds. Because the MODIS phase algorithm is applied to each pixel individually and is not part of a pixel array–based analysis, it is uncertain at this time how best to improve the phase algorithm near cloud edges. Phase discrimination for extremely optically thin cirrus remains problematic.

The data in Figs. 8a and 8b indicate that single cloud layers tend to follow fairly narrow distributions, with some scatter because of variances in macrophysical and optical properties over the extent of the cloud. The data from region B encompass the ARM CART site and are indicative of a more complex cloud structure (Fig. 8c). As with Fig. 8b, a similar identification of the clear-sky pixels and the results of the phase discrimination are presented in Fig. 8d. The data in region B are open to interpretation. The issue here is that, unlike the previous scatterplot in Fig. 8a, these data do not follow rather narrow distributions that can be easily ascribed to a single ice or water cloud model. Baum et al. (1994) showed that some of this ambiguity can be explained by superimposing multilayered cloud radiative transfer

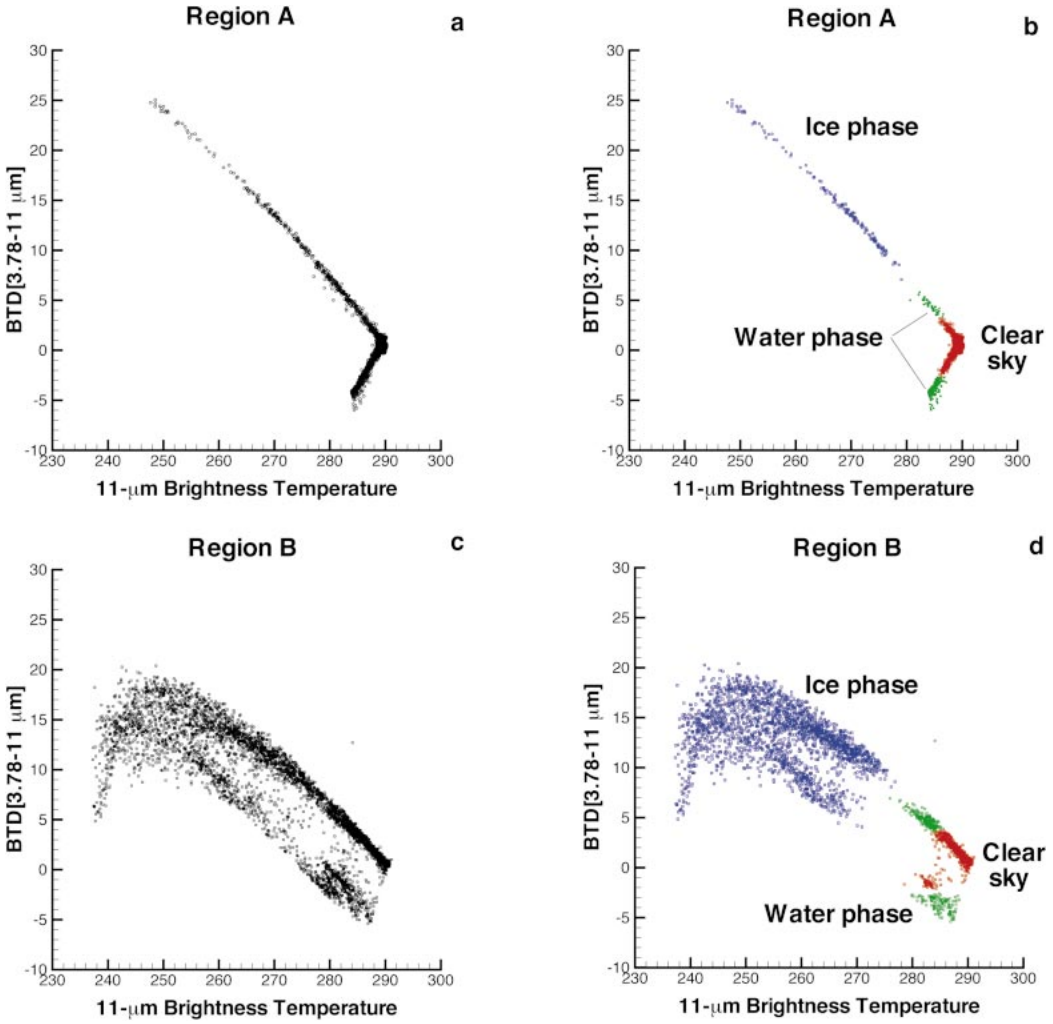

FIG. 8. Radiometric MODIS data from regions A and B are shown. (a) For region A, the BTD(3.78–11 μm) is shown as a function of the 11-μm brightness temperature for the case of two nonoverlapping (i.e., single layered) clouds. (b) The MODIS operational products are used to identify the clear-sky pixels (red), the ice-phase cloud (blue), and the water-phase cloud (green). (c) For region B, the BTD(3.78–11 μm) is shown as a function of the 11-μm brightness temperature for a more complex case containing both single-layered and multilayered clouds. (d) the MODIS operational products are used to identify the clear-sky pixels (red), the ice-phase cloud (blue), and the water-phase cloud (green).

simulations (specifically, cirrus overlying a water cloud) over the data, instead of the more typical single-layered cloud simulations.

Figure 9a shows the single-layered cloud model simulations that are generated using the temperature and humidity data recorded at the ARM site within 1 h of the overpass. The cirrus and water cloud simulations assume cloud-top temperatures of 235 and 287 K, respectively. While only the cold cirrus and cirrus uncinus curves are shown, the other two models provided values that fall between these bounding curves. Results for two single-layered water cloud models (r_{eff} = 4 and 8 μm) are provided additionally. The MODIS data from region B are combined with the RT curves in Fig. 9b. The main point is that the single-layered cloud simulations do not adequately encompass the MODIS data from this region. However, when an additional RT simulation is added (Fig. 9c) for the case of cirrus uncinus overlying a water cloud (r_{eff} = 4 μm; τ_{IR} = 5), the RT simulations almost fully encompass the MODIS data.

In reality, it may be difficult to choose a single representative upper cloud-top temperature. The CO_2-slicing results for region B (not shown) actually display a range of cloud temperatures. For those pixels with 11-μm brightness temperatures less than 250 K, the mean retrieved cloud-top temperature over the region is 243 K with a standard deviation of 3 K. Given some variability in cloud-top temperature, one could superimpose

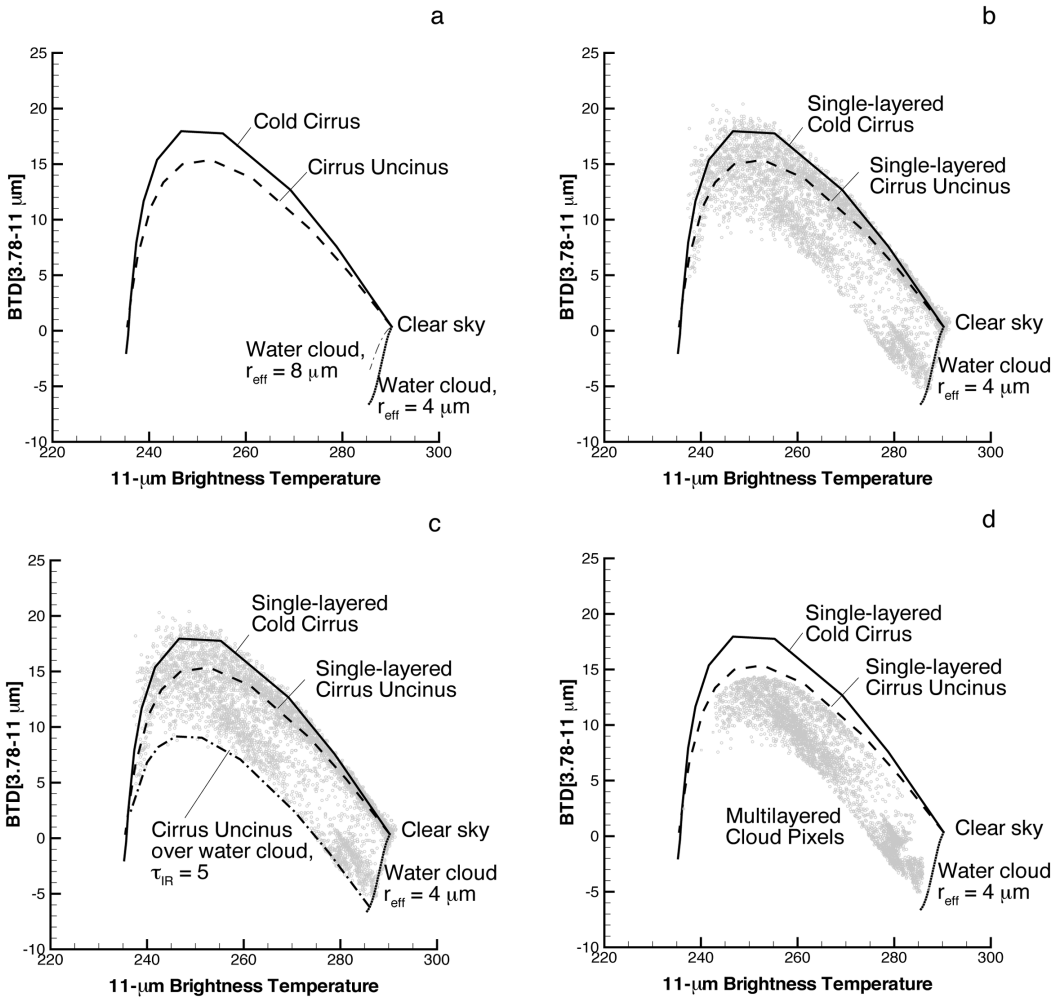

FIG. 9. (a) Radiative transfer simulations for single-layered cirrus and water clouds generated using the rawinsonde data recorded at 0525 UTC at the ARM CART site in Oklahoma. Shown are results for single-layered clouds, consisting of two different cirrus models (cold cirrus and cirrus uncinus) at $T = 235$ K, and a low-level water cloud at 286 K. The MODIS data from region B are superimposed over the (b) RT simulations for single-layered clouds and over the (c) cirrus uncinus overlying a water cloud, where the optical thickness of the underlying water cloud is fixed at $\tau_{IR} = 5$. (d) Pixels are identified as potentially being multilayered.

a number of solutions upon the data, but this would greatly increase the difficulty in interpreting the imagery and would be even more complex of a procedure to automate.

Given the most simplistic interpretation of the scene as being composed of two distinct cloud layers, the pixels thought to contain multiple cloud layers can be separated subsequently from those pixels that lie closely within the ranges of the single-layered cloud curves. The results of this process are shown in Fig. 9d. Even if no further analysis is performed with the pixels associated with more than one cloud layer, the cloud statistics generated from the pixels identified uniquely with the single layers will be more straightforward to understand.

b. 22 April 2001: ARM CART site analyses

The MMCR (see section 2b) radar reflectivity factor (Z_e) height–time cross section shown in Fig. 10 depicts the evolution of the cloud system over the SGP central facility during the night. The upper layer was quite variable with maxima in the 6–7-km layer of 5 dBZ_e. The upper layer was certainly geometrically thick during the hours prior to the *Terra* overpass at 0450 UTC. The data show the layer having a maximal geometrical thickness of 7 km, with cloud bases occasionally extending down to 5.5 km and cloud-top heights reaching up to 13 km. The average cloud-base height during the period was about 6 km, while the echo in the cloud-top region showed a substantial degree of variability with some

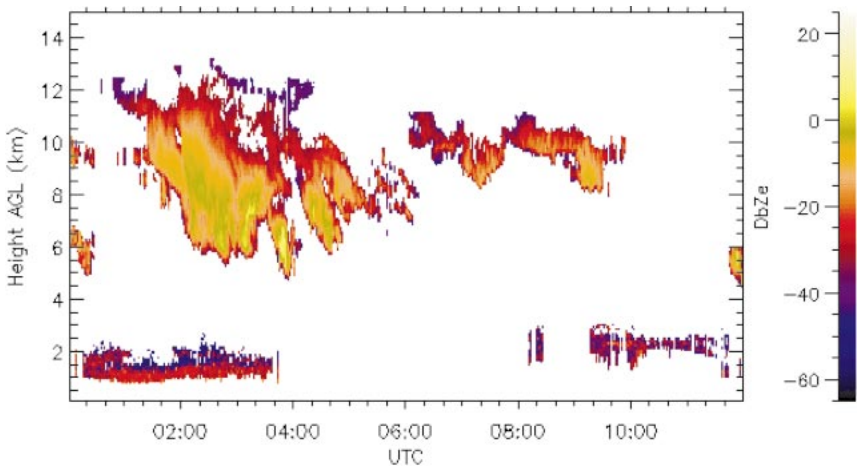

FIG. 10. Height–time cross section of radar reflectivity factor (dBZ_e) observed by the MMCR from 0000 to 1200 UTC 22 Apr 2001.

evidence for multiple cirrus layers above the main cloudy region. The variability in the cloud-top region appears to have been captured correctly by the CO_2-slicing algorithm discussed earlier. Through approximately 0400 UTC, a lower-level cloud layer was observed with a base at 1 km. In the warm boundary layer, insect contamination makes assessment of cloud-top height somewhat uncertain, although the cloud-top height was likely not greater than 2 km (Fig. 10). After approximately 0345 UTC, the lower cloud layer was no longer observed at the SGP central facility and the upper layer gradually became less extensive. At the time of the *Terra* overpass, only a single thin cirrus layer between 7 and 8 km existed over the ARM instruments.

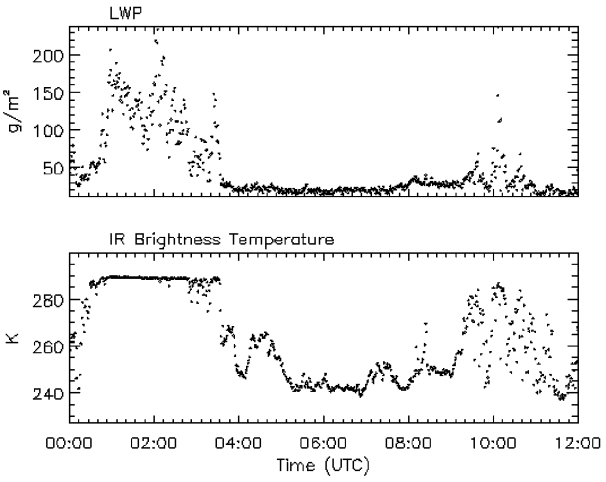

FIG. 11. (a) Liquid water path (LWP, g m^{-2}) derived from brightness temperatures observed by the microwave radiometer at the ARM Southern Great Plains site on 22 Apr 2001. The small residual value near zero after 0400 UTC can be considered zero LWP in this case. (b) IR brightness temperatures calculated from radiances observed by a narrow-field-of-view IR radiometer sensitive to radiation in the 9–11-μm region of the atmospheric window.

Figure 11 shows the variation in the amount of liquid water in the vertical column during the period when the two cloud layers were observed. Although we cannot exclude the possibility that the lower region of the upper cloud layer could be mixed phase, the upper regions of the cloud had temperatures as cold as 210 K. We consider it reasonable to assume that the layer was primarily composed of ice. Doppler fall speeds in the peak Z_e regions of the lower layer were between 1 and 1.5 m s^{-1}, suggestive of large ice crystals that formed through aggregation and vapor deposition in the deep layer above. The lower layer, given that its temperature was well above freezing, was certainly composed of liquid water, and we can, with little uncertainty, ascribe the microwave radiometer–derived liquid water paths entirely to this layer. With maximal LWP amounts of nearly 30 g m^{-2}, this layer is indicative of a nonprecipitating stratocumulus cloud. Cloud property retrieval algorithms applied to the upper (Mace et al. 2002) and the lower layers (Dong and Mace 2003) suggest that the upper cloud layer had maximal absorption optical depths near 5 and would have appeared opaque in the thermal infrared MODIS band. At the time of the *Terra* overpass, the absorption optical depths were less than 1 and the layer would have been considered semitransparent. The lower stratocumulus layer was quite opaque with absorption optical depths near 15.

Only a single cirrus layer existed over the ARM central facility at the time of the *Terra* overpass. If we were to assume the layers advected in a steady state with the mean wind at their altitudes (approximately 20 m s^{-1}), by the time of the *Terra* overpass the back edge of the two-layer system would have been roughly 72 km northeast of the ARM site. This places the back edge of the multilayered system near the northeastern corner of domain B. However, given the nearly saturated state of this low-level atmospheric layer in the sounding launched 45 min after the *Terra* overpass, it is reason-

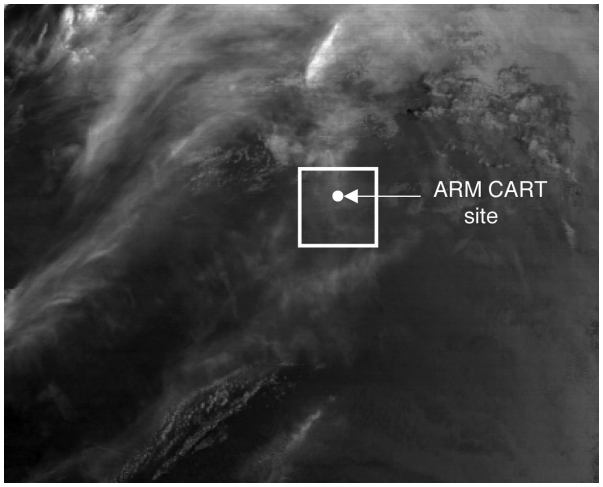

FIG. 12. MODIS 3.78-μm image of a complex nighttime scene recorded at 0455 UTC 28 Mar 2001. The ARM SGP CART site is within the region outlined in the figure. The size of the subregion is 0.43° in latitude by 0.51° in longitude.

able to assume that the lower cloud layer was continuing to persist in the vicinity of the CART site. In fact, the MODIS analysis presented in Fig. 8 supports this idea.

c. Case study: 28 March 2001

A second case study is presented from 0455 UTC 28 March 2001, and a 3.78-μm image of the scene is provided in Fig. 12. The area enclosed by a box (0.43° latitude by 0.51° longitude) represents the region surrounding the ARM SGP CART site and provides the data used in the ensuing analysis. The entire region around the CART site is covered by cloud. This analysis provides enough additional insight as to the problems inherent in the study of nighttime overlapping cloud layers that it merits a brief discussion.

The behavior of the cloud layers from the perspective of the ARM SGP CART site instrumentation in the time period surrounding the MODIS overpass may be seen in Fig. 13. A lower cloud layer with a cloud-top height at 3.5 km (T = 265 K) remains present throughout the entire time period. An upper cloud is also present throughout the time period, with a cloud-top height varying from 8 (T = 233 K) to 10 km (T = 216 K). In the SGP merged-moment product, occasional patches of cloud are present for a brief time period between the uppermost and lowermost cloud layers.

While the ARM SGP CART site merged-moment product indicates the presence of two well-separated (in height) cloud layers, analysis of the MODIS data is more problematic. The MODIS cloud-clearing results indicate that there are no clear-sky pixels in the region. Clear-sky radiances are calculated based on the atmospheric profiles generated each minute at the ARM site from multiple input datasets. The surface temperature at the time of the MODIS overpass is 275.9 K.

Based on these input profiles, a set of radiative transfer calculations was performed, with the results shown in Fig. 14. Two curves, one following the cold cirrus model and the other following the cirrus uncinus model, are provided, assuming a cirrus cloud with no underlying cloud layer. The cloud temperature for these calculations is assumed to be 229 K, and the cloud IR optical thickness ranges from 0 to 10. The lower cloud is assumed to lie at 265 K, consistent with the ARM data. Of note here is that there is no definitive way to infer the phase of the lower cloud layer—it could be ice, water, or a mixture of both. Furthermore, even if a phase is chosen for the lower cloud layer, there is no way to choose a particle size for that layer unambiguously. Two additional curves are provided in the figure, assuming the lower cloud layer is composed of ice (using the cirrus uncinus model) or water (r_{eff} = 8 μm). For this lower cloud layer, the optical thicknesses range between 0 and 20. Note that the BTD(3.78–11) values

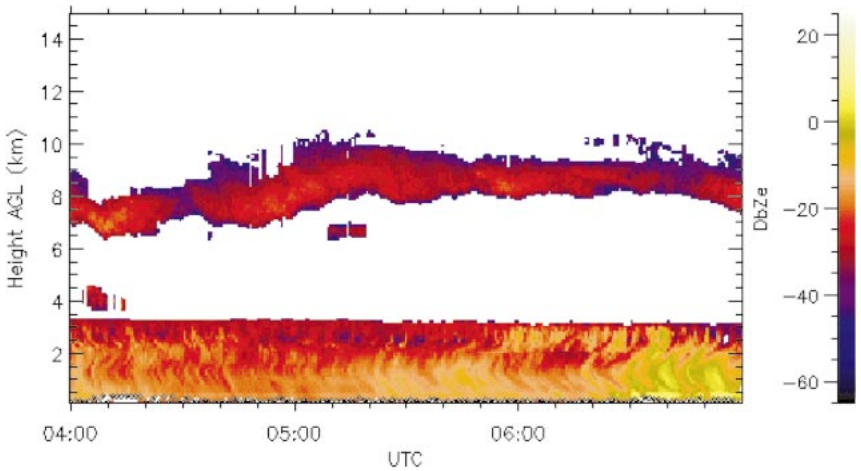

FIG. 13. Height–time cross section of radar reflectivity factor (dBZ_e) observed by the MMCR from 0400 to 0700 UTC 28 Mar 2001.

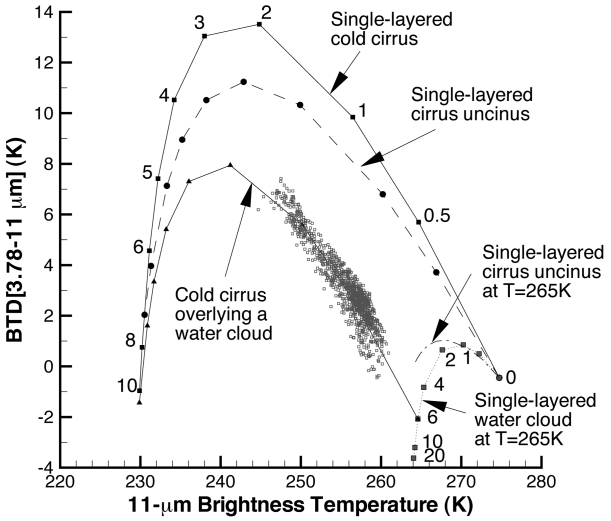

FIG. 14. Radiative transfer simulations for single-layered cirrus and water clouds generated using the atmospheric profile data at 0455 UTC at the ARM CART site in Oklahoma. Shown are results for single-layered clouds, consisting of two different cirrus models (cold cirrus and cirrus uncinus) at $T = 229$ K. Because the lower cloud-layer temperature at cloud top is 265 K, cloud phase is indeterminate. Thus, simulations are shown for both a cirrus uncinus cloud and a water cloud ($r_{\text{eff}} = 8$ μm) at this temperature. A final simulation is provided for cirrus (following the cold cirrus model) overlying a water cloud ($r_{\text{eff}} = 8$ μm; $\tau_{\text{IR}} = 6$). The MODIS data from the subregion shown in Fig. 12 are provided for comparison. All of the MODIS pixels are classified as being multilayered. Infrared cloud-layer optical thickness values (τ_{IR}) are provided for two of the model curves for reference.

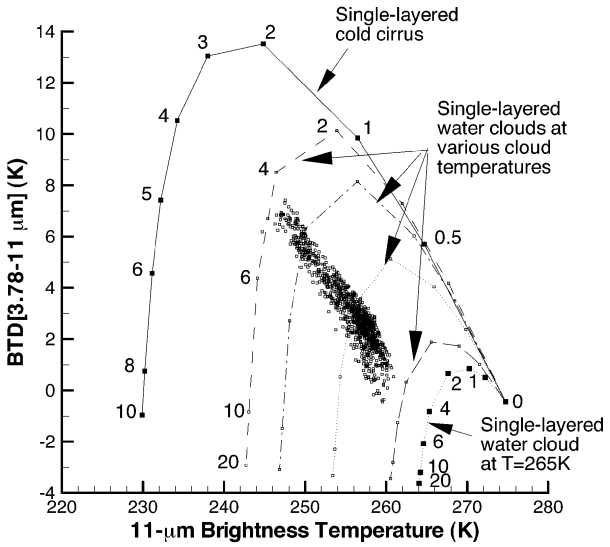

FIG. 15. Radiative transfer simulations for single-layered cirrus and water clouds generated using the atmospheric profile data at 0455 UTC at the ARM CART site in Oklahoma. A single curve was derived using the cold cirrus model at $T = 229$ K, and other curves correspond to water clouds ($r_{\text{eff}} = 8$ μm) at cloud temperatures of 243, 247, 253, 261, and 265 K. The MODIS data from the subregion shown in Fig. 12 are provided for comparison. Infrared cloud-layer optical thickness values (τ_{IR}) are provided on two of the model curves for reference.

for the ice cloud model at high optical thicknesses do not tend to go negative in sign, while they do for the water model. Last, a case is shown of cirrus (following the cold cirrus model) overlying a water cloud ($r_{\text{eff}} = 8$ μm, $\tau = 6$).

The MODIS data from the subsetted region (Fig. 12) are shown for comparison with the radiative transfer calculations. The BTD(3.78–11) values from the MODIS data are much lower, by as much as 5 K, from those values one might expect for a single-layered cirrus cloud. If one extrapolates the MODIS BTD values to a possible cloud temperature, the results are consistent with an ice cloud overlying a water cloud ($r_{\text{eff}} = 8$ μm, $\tau = 6$). The average cloud temperature obtained from the MODIS operational retrieval data product in this subregion is 241 K, which is at least 10 K warmer than the cirrus temperatures one might expect given the cloud heights in the ARM data. However, such a temperature bias is what one might expect when optically thin cirrus overlies a lower cloud layer (Baum and Wielicki 1994). As a final note, all of the pixels in this subregion are identified as being potentially multilayered, using the procedure outlined previously, under the assumption that the lower cloud is water phase.

While it is possible to come up with other combinations of overlapping cloud layers and their inherent properties that might also explain the data, it is unlikely that the MODIS data could be analyzed as clearly with only single-layered cloud models. Figure 15 shows a series of radiative transfer simulations for single-layered water clouds ($r_{\text{eff}} = 8$ μm) at various cloud temperatures, with the MODIS data superimposed. For this case, the MODIS data are oriented orthogonally to the RT simulations. Other simulations of both ice and water clouds having different properties show similar behavior and are not shown. One could envision a retrieval approach where each pixel, or group of pixels, is assigned a cloud height, and then particle size and optical thickness could be inferred. If this approach were taken, the resulting retrievals would be more difficult to interpret, and the range of cloud heights would vary between the lowest and highest cloud layers. It may be simpler to consider all cloud occurrences as being single layered, but, as shown in our analyses, the retrieval results are not optimal for cases in which a thin cirrus overlies a lower cloud layer.

5. Summary

This study reports on recent progress made toward the detection of cirrus overlying lower-level water clouds in nighttime imagery using multispectral data from MODIS. The methodology improvements stem primarily from the availability of more realistic cirrus-scattering models used in the radiative transfer analyses and also the use of operational MODIS products that provide information on whether each pixel contains clouds (i.e., a cloud mask), cloud thermodynamic phase,

and cloud height. Cloud phase is inferred from analysis of the 8.5- and 11-μm data. The updated cirrus-scattering models are now based on mixtures of randomly oriented hexagonal plates and columns, two-dimensional bullet rosettes, and aggregates.

The method uses MODIS near-infrared and infrared bands at 3.78, 8.5, and 11 μm. Cloud-layer discrimination is performed based on analysis of brightness temperature relationships between these bands. The approach first separates clear-sky pixels from those that contain clouds. The MODIS cloud product subsequently provides cloud phase and cloud height for each pixel. Based on the clear-sky and cloud-top radiances, radiative transfer simulations provide relationships for single-layered ice and water cloud layers. An envelope about each single-layered cloud simulation is used to account for instrument noise and variations in individual-layer cloud properties, such as height and effective particle size.

MODIS data that do not fall within the bounds of the single-layered cloud radiative transfer simulations are treated as being multilayered. The most straightforward way to treat the remaining pixels is to assume a two-layer cloud system, wherein the highest and lowest cloud layers found in the data analyses were used to define the bounds for the multilayered cloud radiative transfer simulations. The ARM MMCR data show that the reality of the situation may be quite different. In the first case study analyzed herein, that of 22 April 2001, the upper cloud layer extended upward from a cloud-base height of about 6 km, and sometimes extended to a height of 13 km. Further, there was evidence of multiple cirrus layers. In the second case study, from 28 March 2001, the cloud layers were separated by at least 3 km in height, with only patchy clouds appearing sporadically between the two primary cloud layers.

Because our study is limited to the discrimination between pixels that are single layered and those that have multiple layers, the problem requiring further thought is whether further analysis is possible to infer the microphysical and optical properties of each layer without active sensing measurements, such as a space-based lidar or radar. Under active investigation is the process of automating the methodology outlined herein.

Acknowledgments. This research was supported in part by the Biological and Environmental Research Program (BER), U.S. Department of Energy, Interagency Agreement No. DE-AI02-00ER62901. The authors gratefully thank Kevin Baggett for developing software to facilitate the use of MODIS cloud products in our analyses and Sally Benson for her help in obtaining additional case study data from the ARM SGP CART site. The first author gratefully acknowledges the support of the MODIS and CERES science teams during the course of the research.

REFERENCES

Ackerman, S. A., K. I. Strabala, W. P. Menzel, R. A. Frey, C. C. Moeller, and L. E. Gumley, 1998: Discriminating clear sky from clouds with MODIS. *J. Geophys. Res.*, **103,** 32 141–32 157.

Baum, B. A., and B. A. Wielicki, 1994: Cirrus cloud retrieval using infrared sounding data: Multilevel cloud errors. *J. Appl. Meteor.*, **33,** 107–117.

——, R. F. Arduini, B. A. Wielicki, P. Minnis, and S.-C. Tsay, 1994: Multilevel cloud retrieval using multispectral HIRS and AVHRR data: Nighttime oceanic analysis. *J. Geophys. Res.*, **99,** 5499–5514.

——, D. P. Kratz, P. Yang, S. Ou, Y. Hu, P. F. Soulen, and S.-C. Tsay, 2000a: Remote sensing of cloud properties using MODIS Airborne Simulator imagery during SUCCESS. I. Data and models. *J. Geophys. Res.*, **105,** 11 767–11 780.

——, P. F. Soulen, K. I. Strabala, M. D. King, S. A. Ackerman, W. P. Menzel, and P. Yang, 2000b: Remote sensing of cloud properties using MODIS Airborne Simulator imagery during SUCCESS. II. Cloud thermodynamic phase. *J. Geophys. Res.*, **105,** 11 781–11 792.

Chen, T., Y. C. Zhang, and W. B. Rossow, 2000: Sensitivity of atmospheric radiative heating rate profiles to variations of cloud layer overlap. *J. Climate*, **13,** 2941–2959.

Chou, M.-D., M. J. Suarez, C.-H. Ho, M. Yan, and K.-T. Lee, 1998: Parameterizations for cloud overlapping and shortwave single-scattering properties for use in general circulation and cloud ensemble models. *J. Climate*, **11,** 202–214.

Clothiaux, E. E., M. A. Miller, B. A. Albrecht, T. P. Ackerman, J. Verlinde, D. M. Babb, R. M. Peters, and W. J. Syrett, 1995: An evaluation of a 94-GHz radar for remote sensing of cloud properties. *J. Atmos. Oceanic Technol.*, **12,** 201–229.

——, and Coauthors, 1999: The Atmospheric Radiation Measurement Program cloud radars: Operational modes. *J. Atmos. Oceanic Technol.*, **16,** 819–827.

——, T. P. Ackerman, G. G. Mace, K. P. Moran, R. T. Marchand, M. A. Miller, and B. E. Martner, 2000: Objective determination of cloud heights and radar reflectivities using a combination of active remote sensors at the ARM CART sites. *J. Appl. Meteor.*, **39,** 645–665.

Dong, X., and G. G. Mace, 2003: Profiles of low-level stratus cloud microphysics deduced from ground-based measurements. *J. Atmos. Oceanic Technol.*, **20,** 42–53.

Frey, R. A., B. A. Baum, W. P. Menzel, S. A. Ackerman, C. C. Moeller, and J. D. Spinhirne, 1999: Validation of CO_2-slicing cloud heights computed from MAS radiance data during SUCCESS. *J. Geophys. Res.*, **104,** 24 547–24 555.

Hahn, C. J., S. G. Warren, J. London, R. M. Chervin, and R. Jenne, 1982: Atlas of simultaneous occurrence of different cloud types over the ocean. NCAR Tech. Note TN-201+STR, 212 pp.

——, ——, ——, ——, and ——, 1984: Atlas of simultaneous occurrence of different cloud types over land. NCAR Tech. Note TN-241+STR, 209 pp.

Hogan, R. J., and A. J. Illingworth, 2000: Deriving cloud overlap statistics from radar. *Quart. J. Roy. Meteor. Soc.*, **126,** 2903–2909.

Intrieri, J. M., M. D. Shupe, T. Uttal, and B. J. McCarty, 2002: An annual cycle of Arctic cloud characteristics observed by radar and lidar at SHEBA. *J. Geophys. Res.*, **107,** 8030, doi:10.1029/2000JC000423.

Jakob, C., and S. A. Klein, 1999: The role of vertically varying cloud fraction in the parameterization of microphysical processes in the ECMWF model. *Quart. J. Roy. Meteor. Soc.*, **125,** 941–965.

Kratz, D. P., 1995: The correlated *k*-distribution technique as applied to the AVHRR channels. *J. Quant. Spectros. Radiat. Transfer*, **53,** 501–517.

——, and F. G. Rose, 1999: Accounting for the molecular absorption within the spectral range of the CERES window band. *J. Quant. Spectros. Radiat. Transfer*, **61,** 83–95.

Liang, X.-Z., and W.-C. Wang, 1997: Cloud overlap effects on gen-

eral circulation model climate simulations. *J. Geophys. Res.*, **102,** 11 039–11 047.

Mace, G. G., and S. Benson-Troth, 2002: Cloud layer overlap characteristics derived from long-term cloud radar data. *J. Climate*, **15,** 2505–2515.

——, A. J. Heymsfield, and M. R. Poellot, 2002: On retrieving the microphysical properties of cirrus clouds using the moments of the millimeter-wavelength Doppler spectrum. *J. Geophys. Res.*, **107,** 4815, doi:10.1029/2001JD001308.

Menzel, W. P., W. L. Smith, and T. R. Stewart, 1983: Improved cloud motion wind vector and altitude assignment using VAS. *J. Appl. Meteor.*, **22,** 377–384.

——, D. P. Wylie, and K. I. Strabala, 1992: Seasonal and diurnal changes in cirrus clouds as seen in four years of observations with the VAS. *J. Appl. Meteor.*, **31,** 370–385.

Moran, K. P., B. E. Martner, M. J. Post, R. A. Kropfli, and D. C. Welsh, 1998: An unattended cloud-profiling radar for use in climate research. *Bull. Amer. Meteor. Soc.*, **79,** 443–455.

Morcrette, J.-J., and C. Jakob, 2000: The response of the ECMWF model to changes in the cloud overlap assumption. *Mon. Wea. Rev.*, **128,** 1707–1732.

Salomonson, V. V., W. L. Barnes, P. W. Maymon, H. E. Montgomery, and H. Ostrow, 1989: MODIS: Advanced facility instrument for studies of the earth as a system. *IEEE Trans. Geosci. Remote Sens.*, **27,** 145–153.

Stamnes, K., S.-C. Tsay, W. Wiscombe, and K. Jayaweera, 1988: Numerically stable algorithm for discrete-ordinate-method radiative transfer in multiple scattering and emitting layered media. *Appl. Opt.*, **27,** 2502–2509.

Strabala, K. I., S. A. Ackerman, and W. P. Menzel, 1994: Cloud properties inferred from 8–12-μm data. *J. Appl. Meteor.*, **33,** 212–229.

Stubenrauch, C. J., A. D. Del Genio, and W. B. Rossow, 1997: Implementation of subgrid cloud vertical structure inside a GCM and its effect on the radiation budget. *J. Climate*, **10,** 273–287.

Tian, L., and J. Curry, 1989: Cloud overlap statistics. *J. Geophys. Res.*, **94,** 9925–9935.

Uttal, T., E. E. Clothiaux, T. P. Ackerman, J. M. Intrieri, and W. L. Eberhard, 1995: Cloud boundary statistics during FIRE II. *J. Atmos. Sci.*, **52,** 4276–4284.

Weare, B. C., 1999: Combined satellite- and surface-based observations of clouds. *J. Climate*, **12,** 897–913.

——, 2001: Effects of cloud overlap on radiative feedbacks. *Climate Dyn.*, **17,** 143–150.

Wielicki, B. A., and J. A. Coakley Jr., 1981: Cloud retrieval using infrared sounder data: Error analysis. *J. Appl. Meteor.*, **20,** 157–169.

Wylie, D. P., and W. P. Menzel, 1999: Eight years of high cloud statistics using HIRS. *J. Climate*, **12,** 170–184.